Nano Energy 78 (2020) 105239

Contents lists available at ScienceDirect

Nano Energy

journal homepage: http://www.elsevier.com/locate/nanoen

Stabilizing surface chemical and structural Ni-rich cathode via a non-destructive surface reinforcement strategy

Kai Yuan [a,1], Nan Li [a,b,1], Ruiqi Ning [a], Chao Shen [a,**], Nan Hu [a], Maohui Bai [a], Kun Zhang [a], Zhanyuan Tian [c], Le Shao [c], Zhaowen Hu [c], Xin Xu [b], Ting Yu [b,***], Keyu Xie [a,*]

[a] State Key Laboratory of Solidification Processing, Center for Nano Energy Materials, School of Materials Science and Engineering, Northwestern Polytechnical University and Shaanxi Joint Laboratory of Graphene (NPU), Xi'an, 710072, PR China
[b] Division of Physics and Applied Physics School of Physical and Mathematical Sciences, Nanyang Technological University, 637371, Singapore
[c] Shaanxi Coal and Chemical Technology Institute Co., Ltd, Jinye Road, Xi'an, 710070, PR China

ARTICLE INFO

Keywords:
Plasma treatment
Ni-rich cathode
Precursor
Structure
Li-ion batteries

ABSTRACT

Surface chemistry and micro/nano-structure of precursors greatly determine the characteristics and performances of precursor-derived Ni-rich cathodes. Some progress has been achieved in pre-treating precursors via classical wet-chemical methods, nevertheless, it is still inevitable that the surface chemical components or structures of precursors will be changed. Thus, exploring the non-destructive surface reinforcement strategy is of vital importance. Taking the typical Ni-rich cathodes ($LiNi_{0.8}Co_{0.15}Al_{0.05}O_2$, NCA) as an example, herein, a non-destructive surface reinforcement strategy to tailor surface characteristics of the precursor through plasma treatment technique has been proposed. Impressively, spectroscopic analysis and atomic-level imaging reveal that the plasma treatment of precursor is beneficial for both promoting the conversion of Ni^{2+} to Ni^{3+} and the formation of a porous surface without crystal defects. As a result, the annealed high-crystallinity NCA cathode, without NiO-type rock salt phase on the surface, displays enhanced cycling stability (81.2% capacity retention at 1C over 200 cycles) and increased rate performances (161.1 mA h g^{-1} at 5C). The feasibility of extending this strategy to other electrode materials (such as $LiNi_xCo_yMn_{1-x-y}O_2$, $LiNiO_2$, etc.) by sintering precursors further promises a bright future. This work provides guidance to rational modify the Ni-based cathode materials and hold great potential of reviving the next generation high-energy-density Li-ion batteries.

1. Introduction

Surface chemistry and micro/nano-structures of materials, mainly influenced by the surface chemical properties and morphologies of precursors, significantly determine its performance in catalysis and energy storage [1,2]. In particular, the electrochemical performance of Li-ion battery (LIB) cathode materials are greatly dependent on the valence state, crystal structure, and adsorbates of the precursor surface [3,4]. Therefore, enhancing the fundamental understanding of the relationship between precursor surface properties and the electrochemical performances of cathode materials could provide new insights for improving performances of LIBs.

Ni-rich layered oxides, such as $LiNi_xCo_yAl_{1-x-y}O_2$ ($x > 0.7$, NCA) and $LiNi_xCo_yMn_{1-x-y}O_2$ ($x > 0.7$, NCM), are considered as the most attractive cathode materials of LIBs to meet the requirement for high-energy-density applications, such as electric vehicles (EVs), due to their high theoretical capacity (~270 mA h g^{-1}) and low cost [5,6]. Unfortunately, inherent poor cycling stability during the repeated charge/discharge processes remains a daunting challenge in their practical applications. Previous researches reveal that the NiO-type rock salt phase is formed on the surface of Ni-rich layered oxides, resulting in the poor cycling stability. Furthermore, the irreversible migration of Ni^{2+} to lithium (Li) positions (cation mixing), which is the cause of the formation of NiO-type rock salt phase, leads to the surface reconstruction and the structural evolution from the surface to the interior of Ni-rich layered oxides [7–13]. Therefore, it is of great significance to explore an

* Corresponding author.
** Corresponding author.
*** Corresponding author.
E-mail addresses: shenchao@nwpu.edu.cn (C. Shen), yuting@ntu.edu.sg (T. Yu), kyxie@nwpu.edu.cn (K. Xie).
[1] These authors contributed equally to this work.

https://doi.org/10.1016/j.nanoen.2020.105239
Received 24 June 2020; Received in revised form 26 July 2020; Accepted 28 July 2020
Available online 13 August 2020

effective surface modification method of Ni-rich layered oxides.

Ni-rich cathodes is supposed to inherit the structural characteristics of the precursor, such as the symmetry, primary particle arrangements, and genetic orientation properties [4,14–16]. During the preparation of the Ni-rich cathode materials, Ni^{2+} in the precursor is partially oxidized to Ni^{3+}, and partially retained on the surface of the obtained product, due to the high energy barrier of the oxidation process [15–18]. In addition, crystal defects on the surface of the precursor may be inherited on the surface of cathodes [14]. Thus, fulfilling optimization on structure and chemical properties of the precursors can be regarded as an effective method to realize the modification of cathode materials. In recent years, some progress about the precursor pre-treatment based on wet chemistry, via the widely used $Na_2S_2O_8$ and $KMnO_4$ oxidants, has been reported and has achieved the certain effect [14,19–23]. However, these approaches are not suitable for practical applications owing to the following reasons: (1) The reduction product SO_4^{2-} of $Na_2S_2O_8$ will insert into the precursor to maintain charge balance. The increased sulfur species will give rise to some parasitic effects on the cathode materials. For example, the superfluous of sulfur species ($LiSO_3^-$ and $LiSO_4^-$) may facilitate the formation of nanopores in the cathode materials and accelerate the disintegration of the secondary particles [24]. (2) $KMnO_4$ oxidant may cause Mn doping on the surface of precursors, resulting in more serious Li^+/Ni^{2+} mixing, which violates the original intention of pre-oxidation. (3) Repeated cleaning steps not only increase the complexity of the process but also lead to an increased cost of these materials as well. Therefore, it is essential to design a simple, effective, and non-destructive precursor surface treatment strategy which can change the chemical properties and structures of the surface of precursor (such as Ni^{2+} content and surface layered structure) under the premise of maximizing the capacity, and inhibits the formation of NiO-type rock salt layer on the surface of Ni-rich cathode materials simultaneously.

Plasma treatment, by employing excited, dissociated, and ionized gas molecules, has been regarded as a high-efficient and environmentally friendly surface treatment technology in the area of powder processing and surface engineering [25–27]. Oxygen is one of the most widely used electronegative gases in plasma treatment. With the electron energy of 6.70–12.00 eV, its ability to capture electrons is strong, which leads to the easy breakage of its molecular bonds and the formation of high-energy active groups (O,·OH, O_3·, O_3). When these reactive groups contact with reduced nickel components of precursors, the oxidation of $Ni^{2+} \rightarrow Ni^{3+}$ can be achieved. Herein, a general and non-destructive precursor surface reinforcement strategy, plasma treatment, has been proposed. An ideal surface with regular layered nickel oxide hydroxide (NiOOH) phase can be achieved on the precursors through plasma treatment process. The Ni-rich layered oxides without the NiO-type rock salt phase can be obtained during the following calcination process, which are proved by the spectroscopic analysis and atomic level imaging. Compared with the untreated counterpart, $LiNi_{0.8}Co_{0.15}Al_{0.05}O_2$ (PTNCA) prepared via plasma treatment delivers enhanced cycling stability (81.2% capacity retention at 1C over 200 cycles) and better rate capability (161.1 mA h g^{-1} at 5C). This strategy also exhibits its good feasibility of being extended to other Ni-rich cathodes, such as $LiNi_{0.8}Co_{0.1}Mn_{0.1}O_2$. As a significant breakthrough over the previously reported methods, this strategy enhances the chemical/structural stability of such layered oxides without any damages on the surface of particles, and therefore hold great potential of reviving Ni-rich cathodes further.

2. Experimental section

2.1. Material fabrications

$LiNi_{0.8}Co_{0.15}Al_{0.05}O_2$ (NCA) and $LiNi_{0.8}Co_{0.1}Mn_{0.1}O_2$ (NCM) were prepared by a solid-state reaction of commercial Ni-rich precursors of $Ni_{0.8}Co_{0.15}Al_{0.05}(OH)_2$ (NCA-p) and $Ni_{0.8}Co_{0.1}Mn_{0.1}(OH)_2$ (NCM-p). These precursors were thoroughly mixed with $LiOH{\cdot}H_2O$ at the molar ratio of 1:1.05. Then the mixture was calcined at 480 °C for 6 h and further at 750 °C for 12 h under the atmosphere of oxygen in a tube furnace. To acquire the plasma-treated precursor, the commercial precursors (NCA-p and NCM-p) were placed in a plasma furnace, treated at a mixing atmosphere of O_2/Ar (2:1 in volume) for 5 times (3 min per time). After repeated 5 times, the powders completely changed from green to black and the plasma-treated precursors (PTNCA-p and PTNCM-p) were obtained. Then the plasma-treated precursors were mixed with $LiOH{\cdot}H_2O$ and calcined under the same conditions of NCA and NCM to get the plasma-treated $LiNi_{0.8}Co_{0.15}Al_{0.05}O_2$ (PTNCA) and $LiNi_{0.8}Co_{0.1}Mn_{0.1}O_2$ (PTNCM).

2.2. Characterizations

Scanning electron microscope (SEM) and transmission electron microscopy (TEM) measurements were carried out with FEI Nano SEM 450 and JEOL JEM-2100F, respectively. X-ray diffraction (XRD) patterns were carried out with an X'Pert PRO MPD (Cu Kα radiation, 0.15406 nm) at room temperature. The structural parameters were obtained by the Rietveld Refinement method with the General Structure Analysis System (GSAS) program using the model of $R\bar{3}m$ space group [28]. The XRD patterns for Rietveld Refinement were obtained with a Bruker D8 X-ray diffractometer (Cu Kα radiation, 0.15406 nm) in the 2θ range of 10–80° with a step size of 0.2° min^{-1}. X-ray photoelectron spectroscopy (XPS) was carried out with ESCALAB 250Xi, Thermo Scientific. The distribution of pore size and specific surface area of NCA-p, PTNCA-p, NCA, and PTNCA were determined by an ASAP-2020 surface area analyzer through using the methods of Brunauer-Emmett-Teller (BET) and Barrett-Joyner-Halenda (BJH), respectively. 10 g cathode material was dispersed in 100 ml water, stirred for 5 min, and the METTLER pH meter FE28 was used to collect the pH value of NCA and PTNCA. Double Spherical Aberration Corrector Transmission Electron Microscope, collected on FEI Themis Z, was used to investigate the surface structures of NCA and PTNCA. And the STEM-HAADF imaging was obtained with a convergence angle of 28.6 mrad from 75 to 200 mrad.

2.3. Electrochemical characterization

The active material, poly (vinylidene fluoride) (PVDF), and acetylene black were mixed at the mass ratio of 8:1:1 in N-methyl-2-pyrrolidone (NMP), and stirred for 6 h. Afterward, the formed slurry was coated on aluminum foil and dried at 120 °C in a vacuum oven overnight, which was punched into working electrodes with a diameter of 12 mm. The prepared electrodes were used as working electrodes, and metallic lithium foils were used as the counter electrodes and reference electrodes. The electrolyte is 1 M $LiPF_6$ in the mixture of ethylene carbonate (EC), dimethyl carbonate (DMC), and ethyl methyl carbonate (EMC) (1:1 in volume). The CR2032-coin-type cells were assembled with Celgard 2500 as the separator in the argon-filled glovebox with the concentrations of moisture and oxygen below 0.1 ppm. The cathode mass loading is ~2 mg cm^{-2} and the amount of electrolyte used for each cell is around 80 μ (electrolyte volume: cathode material weight = 1 L: 25 g). The electrochemical impedance spectroscopy (EIS) was performed with an AC perturbation voltage of 5 mV during the frequency range of 10^{-2} Hz–10^5 Hz. The LAND CT2001A battery test instrument was used to perform galvanostatic charge/discharge curves at different current densities with voltage window of 2.8–4.3 V and 2.8 - 4.5 V(*vs.* Li^+/Li).

3. Results and discussion

Fig. 1 illustrates the plasma-treated process of Ni-rich layered oxide precursors. The precursor prepared by coprecipitation was placed in a plasma furnace and treated at a mixing atmosphere of O_2/Ar (2 : 1 in volume) for 5 times (3 min per time). During this process, the voids between the primary particles are fully exposed after the treatment of

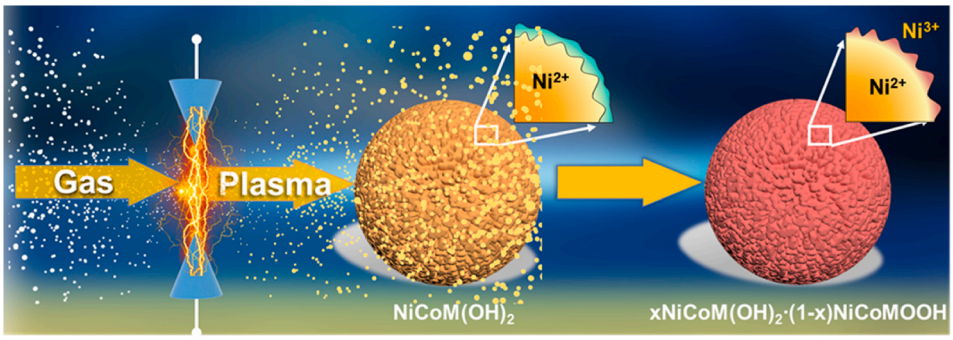

Fig. 1. Schematic illustration of the plasma treatment process of the precursor.

the O_2-based plasma, and a layer of NiOOH phase with an ordered crystal structure was formed on the surface simultaneously. After repeating 5 times, the plasma-treated precursor (PTNCA-p/PTNCM-p) was obtained. Afterward, PTNCA-p/PTNCM-p and $LiOH{\cdot}H_2O$ were mixed and calcined at 750 °C for 12 h under O_2 atmosphere to obtain the modified Ni-rich layered oxides (PTNCA/PTNCM).

As can be seen from Fig. 2a,d, approximately 50 g of NCA precursors (NCA-p) and PTNCA-p powder containing inside two transparent sample bags show clear color changes from bright green for NCA-p to completely black for PTNCA-p after plasma treatment. The typical macroscopic morphologies of NCA-p and PTNCA-p are investigated by scanning electron microscopy (SEM). As shown in Fig. 2b,e, the diameters of both NCA-p and PTNCA-p spherical secondary particles are located in the range of 7–17 μm. It is worth noting that without gold plating, the obvious charging effect can be observed from Fig. 2b owing to the severe aggregation of charge, which indicates the poor conductivity of NCA-p. On the contrary, the high-quality image with a clear hierarchy, strong three-dimensional sense, and high-resolution can be obtained in Fig. 2e, which reveals the conductivity of PTNCA-p is significantly improved after plasma treatment. In addition, the conductivity is investigated by using a four-probe meter (Figs. S1a–c). The NCA-p displays a much higher impedance of 136.07 kΩ, while a greatly reduced impedance of 0.18 kΩ was obtained after the plasma treatment, which may be attributed to the formation of a new conductive phase on the surface of PTNCA-p particles. Furthermore, a blurred layer can be observed on the surface of the NCA-p (as marked by the orange dashed line in Fig. 2c), while a fine image of the surface of the PTNCA-p is obtained, and the voids between the primary particles are fully exposed (Fig. 2f), which may be due to the etching effect of plasma on the surface of NCA precursors. The exposure of the voids between the primary

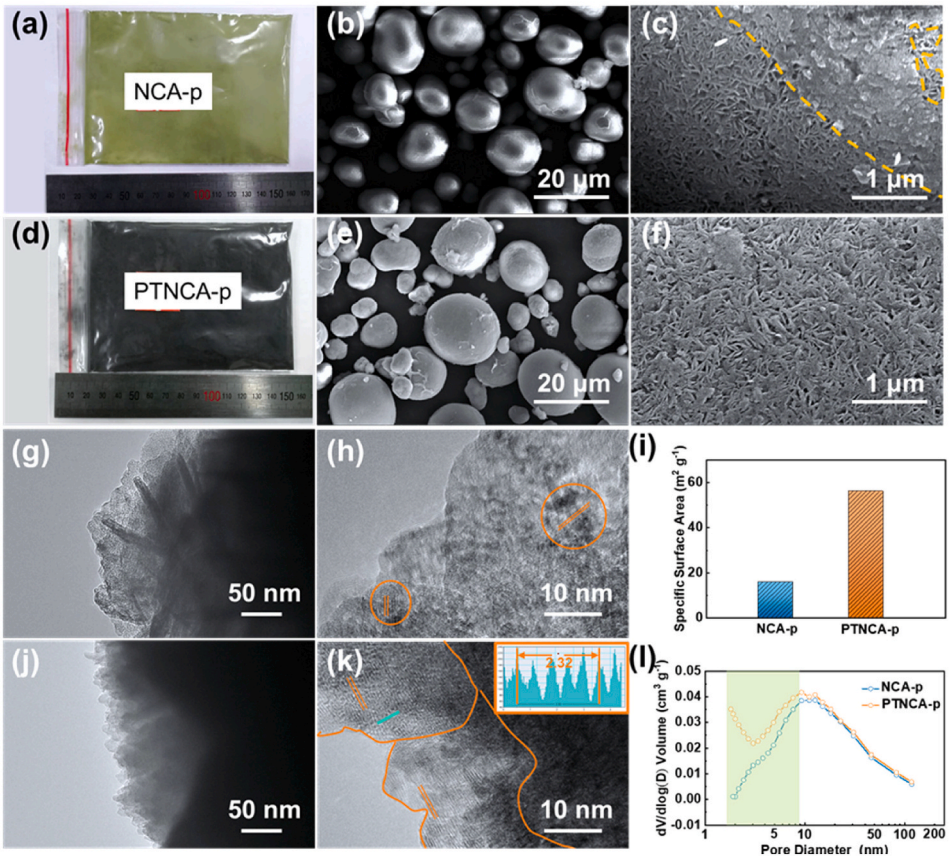

Fig. 2. Morphology and structure characterizations of plasma treated NCA precursor. a,d) Photographs of NCA-p and PTNCA-p, respectively. Top-view SEM images of b,c) NCA-p and e,f) PTNCA-p, respectively. g,h) TEM and HRTEM images of NCA-p. j,k) TEM and HRTEM images of PTNCA-p. i,l) The specific surface area and the corresponding pore-size-distribution profile of NCA-p and PTNCA-p.

particles facilitates the penetration of molten LiOH during the subsequent calcination, resulting in a reduction of lithium residue on the surface of the cathode materials, as well as the uniform distribution of primary particles [19].

The transmission electron microscopy (TEM) and high-resolution TEM (HRTEM) are performed to further investigate the oxidation and etching effect of plasma on the surface of precursors. Nanocrystals with various orientation appear in NCA-p (as marked by orange circles in Fig. 2h), indicating heterogeneous phases on the surface of NCA-p [15, 19]. In contrast, as can be seen from Fig. 2g,j, the contour of PTNCA-p is much rougher than that of NCA-p. A uniform crystal phase with the thickness of ~23 nm appears on the surface of PTNCA-p, and the crystal plane is perpendicular to the normal of the secondary sphere (Fig. 2k). The surface of PTNCA-p displays the layered structure without NiO-type rock-salt phase. The spacing of this newly formed phase is 0.46 nm, which is consistent with the (001) plane of NiOOH, indicating the formation of NiOOH outer layer on the surface of PTNCA-p. During the subsequent solid reaction, NiOOH can be easily converted into NCA with a fine layered structure [29]. The specific surface area and pore-size-distribution of NCA-p and PTNCA-p are investigated by nitrogen adsorption-desorption measurements. As shown in Fig. 2i, the BET specific surface area of PTNCA-p is 56.6807 $m^2\ g^{-1}$, three times larger than that of NCA-p (16.3046 $m^2\ g^{-1}$), and the pore size distributions of both NCA-p and PTNCA-p are mainly in the range of 2–120 nm (Fig. 2l) according to the Barrett-Joyner-Halenda model. It is worth noting that the pore size distribution curve of PTNCA-p is substantially consistent with that of NCA-p, while the pore volume of PTNCA-p is significantly higher than that of NCA-p in the range of 2–10 nm, which may be the reason of the enhanced specific surface area of PTNCA-p. As shown in Figs. S2c and d, the specific surface areas of NCA and PTNCA are 0.2341 $m^2\ g^{-1}$ and 0.5327 $m^2\ g^{-1}$, respectively, indicating that the specific surface area of these two materials is not significantly different. These results verify the previous inferences about the beneficial effects of plasma treatment.

To further explore the effects of plasma treatment on the calcined materials, the morphological, structural, surface chemical, and electrochemical properties of NCA and PTNCA are investigated. As can be seen from Fig. 3a,c, the secondary particles of both NCA and PTNCA display the similar microsphere morphology with a diameter of about 10 μm after solid-state reacting with LiOH. However, it should be noted that the size of primary particle of PTNCA is in the range of 300–800 nm (Fig. 3d), significantly larger than that of NCA (300–600 nm, Fig. 3b), which can be attributed to the fact that the voids between the primary particles of the plasma-treated precursors are completely exposed. Exposed voids will facilitate the diffusion of molten LiOH during the calcination progress and provide sufficient space for the further growth of the primary particles [30,31]. In addition, the pH of NCA and PTNCA are 11.7 and 11.4 respectively, indicating less residue of LiOH and Li_2CO_3 on the surface of the cathode materials. TEM images of the secondary particles shows the consistent morphology with Fig. 3e,g and Fig. S3. In addition, elements of Ni, Co, and Al on both NCA and PTNCA particles are uniformly distributed (Fig. 3e,g), which indicates that the plasma treatment does not influence the distribution of these three elements of the Ni-rich materials. To confirm crystal structures of the surfaces of NCA and PTNCA, TEM and HRTEM are carried out. NCA exhibits a disordered outer layer with the thickness of 3 nm, which will block the Li^+ diffusion pathway and thus lead to the poor cycling performance (Fig. 3h and i). And this layer also slightly hinders the transfer of electrons (Figs. S1d–e). Impressively, PTNCA exhibits a continuous layered structure with the $R\bar{3}m$ space group from the bulk to the surface, and no secondary phase is observed at the particle surface (Fig. 3k,l), which hold great potential to facilitate the diffusion of Li^+ at the surface of particle, and thus enhance the cycling stability.

To further investigate the effect of plasma treatment on the structure of Ni-rich cathode materials, the structural details of the surface of NCA and PTNCA are explored by atomic-resolution Z-contrast scanning transmission electron microscopy-high-angle annular dark-field (STEM-HAADF) imaging. In the imaging, lithium atoms cannot be detected due to its light weight, and the bright spots represent transition metal atoms. The surface of NCA can be divided into two different regions (Fig. 4a). The bulk (region 1) displays a well-ordered layered structure with the regular arrangement of lithium and transition metal atoms, while in the outer surface (~3 nm, region 2), the transition metal atoms appear at the Li sites and form rock-salt phase, which is attributed to the irreversible migration of Ni cations to Li sites and could block the lithium ion diffusion channel, then decrease electrochemical performances [32]. In contrast, the maintained layered structure with obvious lithium ion diffusion channels can be observed from bulk to surface in the PTNCA sample, as marked by the white arrow in Fig. 4b. HAADF imaging (Fig. 4c–e) are performed to obtain more details of the layered regions and the rock-salt phase region on the surface of NCA and PTNCA. The corresponding line intensity profiles of the lithium layer and transition metal layer are detected, as shown in Fig. 4f–h. No obvious transition metal ion signal is detected along the yellow arrow in the lithium layer of region 1 (Fig. 4c,f), indicating that Li^+ sites are not occupied by the transition metal cations. Unfortunately, some bright dots are observed in the space between two transition metal layers of region 2 (Fig. 4d), which indicates that the positions of Li^+ may be occupied by some other atoms because lithium atoms are not visible in the atomic-level HAADF image of the prior art. Further confirmation through the line intensity distribution of the transition metal ion reveals that the dots represent the transition metal cations (Fig. 4g), which indicates that the transition metal cations migrated into the lithium diffusion channel along the

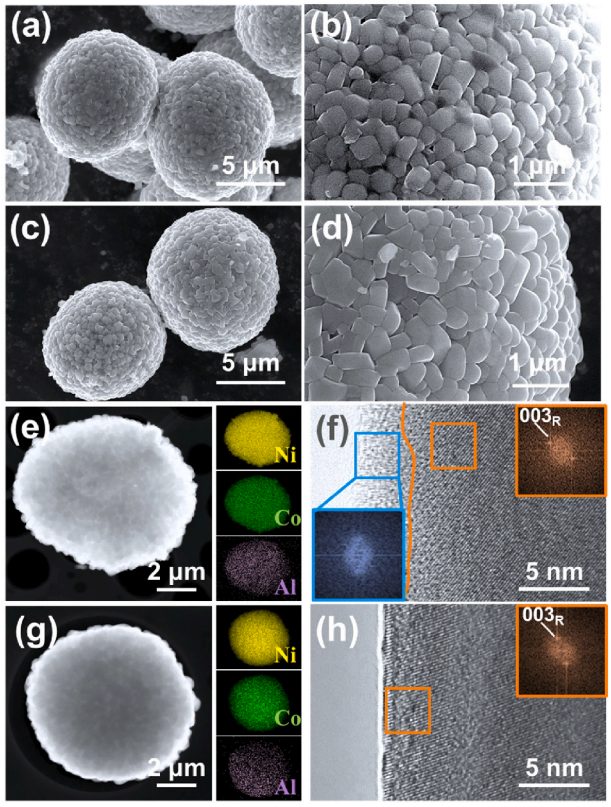

Fig. 3. Morphology and structure characterizations of NCA and PTNCA. a,c) SEM images of NCA and PTNCA, respectively. b,d) Magnified views of a,c) respectively. e,g) TEM images and corresponding elemental mapping of Ni (yellow), Co (green), and Al (purple) elements of NCA and PTNCA, respectively. f,h) TEM images of NCA and PTNCA with corresponding FFT patterns for different regions (insets). (For interpretation of the references to color in this figure legend, the reader is referred to the Web version of this article.)

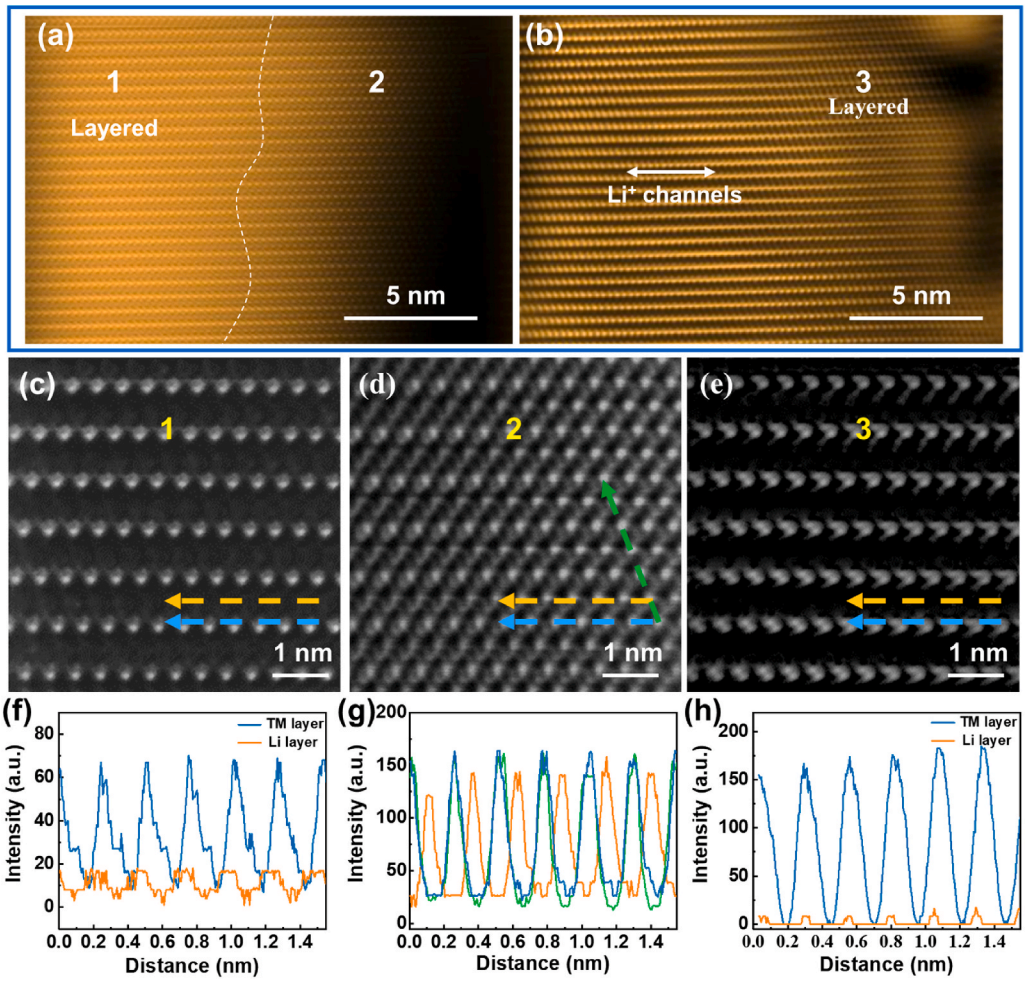

Fig. 4. a,b) STEM-HAADF images of NCA and PTNCA, respectively. c-e) Detailed structural information of different regions of NCA and PTNCA. f-h) The corresponding line intensity profiles of the layers labeled with arrows in c-e.

yellow and green arrows, leading to the formation of NiO-type rock salt phase. In contrast, the obvious layered structure on the surface of PTNCA can be observed (Fig. 4e,h), indicating the Li^+ site is not occupied by the transition metal cation and the diffusion path of lithium ion is maintained. The structure of PTNCA is well-matched with $LiMO_2$ of the $R\bar{3}m$ space group under the <010> region projection.

The powder X-ray diffraction (XRD) is conducted to investigate the structural changes after plasma treatment. As shown in Fig. 5a, the XRD patterns of NCA-p and PTNCA-p are generally consistent with the Ni $(OH)_2$ phase (JCPDS card no. 14–0117) [20]. .However, as shown in Fig. 5a, a new signal at $2\theta = 37.3°$ appears in the XRD pattern of PTNCA-p (the patterns in the 2θ range of 35-40° shown in Fig. S4), corresponding to the (002) plane of the NiOOH phase (JCPDS card No. 03–0141) [29,33], which indicates the NiOOH phase with an ordered crystal structure is formed on the surface of PTNCA-p after plasma treatment. In addition, the typical peaks of PTNCA-p are slightly widened and shifted to a higher angle, which also indicates the generation of NiOOH crystal phase [15]. The results of XRD are consistent with those observed in the HRTEM image of PTNCA-p (Fig. 2k). The Bragg reflections and refinement results of NCA and PTNCA are consistent with the $R\bar{3}m$ space group, which exhibits a typical hexagonal α-$NaFeO_2$ structure (Fig. 5b, Fig. S5). The splitting of (006)/(012) and (018)/(110) bimodal in both patterns is obvious, revealing the well-layered structure in both NCA and PTNCA [34]. Furthermore, it is worth noting that the intensity ratio of (003) peak and (104) peak ($I_{(003)}/I_{(104)}$) displays a negative correlation with the degree of cation mixing, i.e., the higher the value of $I_{(003)}/I_{(104)}$, the lower the degree of Li^+/Ni^{2+} mixing [35]. The values of $I_{(003)}/I_{(104)}$ of NCA and PTNCA are 1.43 and 1.87, respectively (Fig. 5c). It can be seen from the Rietveld refinement results (Table S1) that the occupancies of Ni in Li site in PTNCA (3.520%) is lower than that in NCA (4.058%). These results suggest that PTNCA possesses a well-ordered layered structure and a lower degree of Li^+/Ni^{2+} mixing than NCA.

To further investigate the chemical structures of the surface of PTNCA, X-ray photoelectron spectroscopy (XPS) is carried out to detect the valence state of Ni in both NCA and PTNCA. As can be seen from Fig. 5d and e, the Ni 2p spectra of NCA-p and PTNCA-p reveal two valence state of Ni: Ni^{3+} (~856.5 eV) and Ni^{2+} (~855 eV) [36]. The content of Ni^{3+} on the surface of PTNCA-p is 60.3%, much larger than that of NCA-p (38.1%), which indicates the content of Ni^{3+} can be greatly enhanced after plasma treatment. As shown in Fig. 5g and h, the content of Ni^{3+} on the surface of PTNCA is further increased to 75.4%, significantly larger than that of NCA (64.2%), revealing the degree of Li^+/Ni^{2+} mixing is greatly reduced and the well-ordered layered structure can be obtained. And the high-resolution O 1s spectrum of PTNCA-p (Fig. S6b) can be separated into three peaks at 529.0 eV for NiOOH, 530.7 eV for NO–OH, and 531.9 eV for H_2O, respectively [37]. Obviously, the O 1s spectrum of NCA-p (Fig. S6a) has two peaks at 530.4 eV for $Ni(OH)_2$ and 531.4 eV for H_2O [38]. In order to further confirm the influence of plasma treatment on precursors and calcined products, XPS depth profiles of NCA-p, PTNCA-p, NCA and PTNCA were collected (Fig. S7). To further demonstrate the effect of plasma treatment along the depth of precursors and calcined products, the intensity difference of

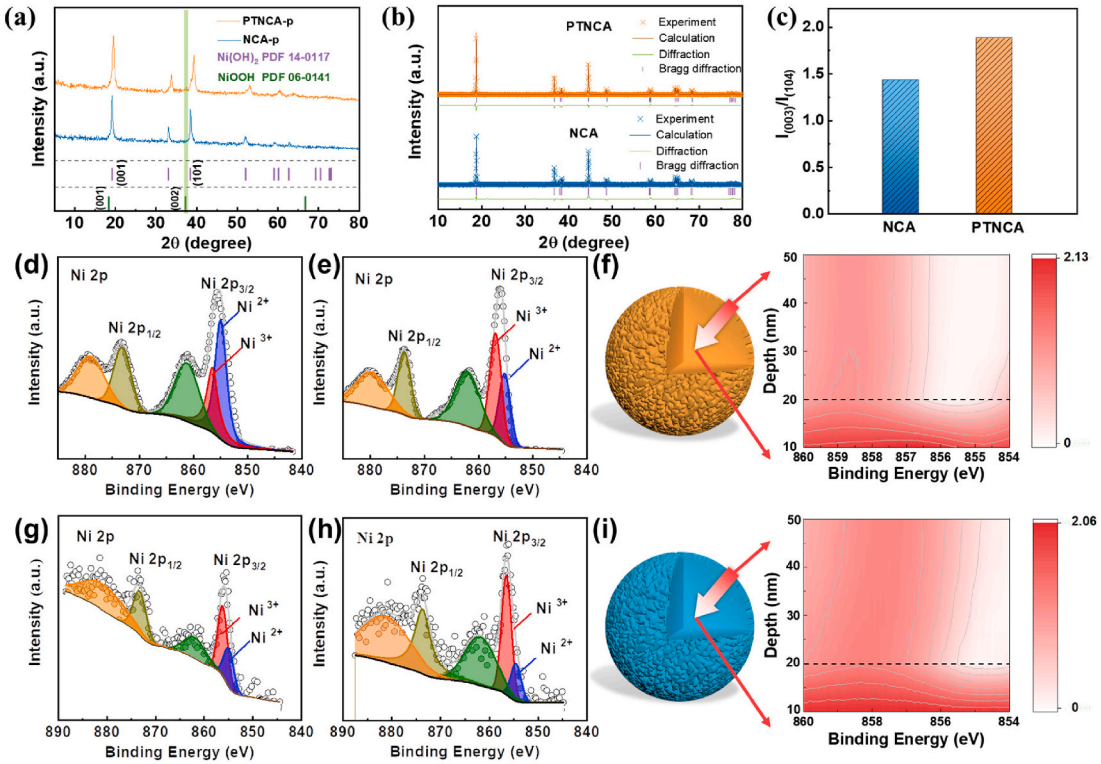

Fig. 5. XRD patterns of a) NCA-p and PTNCA-p, and b) Rietveld refinement of NCA and PTNCA. c) Comparison of the $I_{(003)}/I_{(104)}$ of NCA and PTNCA. XPS spectra on the surface of d) NCA-p, e) PTNCA-p, g) NCA, and h) PTNCA, respectively. The intensity differences of the XPS signals between f) NCA-p and PTNCA-p, as well as i) NCA and PTNCA along the depth direction.

XPS signals between NCA-p and PTNCA-p, as well as NCA and PTNCA at the same depth are collected (Fig. 5f,i), respectively. The magnitude and fluctuations of the difference in the graph represent the offset of the peak position. It can be seen that the peak of PTNCA-p shifts to high energy and the difference is obvious in the range of 10–20 nm, while the difference becomes inconspicuous when the depth is greater than 20 nm (Fig. 5f), which indicates that the depth of plasma treatment remains approximately 20 nm. Similar results can be obtained in the differences of XPS spectra between NCA and PTNCA at the same depth (Fig. 5i).

To evaluate the electrochemical performances of cells incorporating plasma treated Ni-rich cathodes, PTNCA|Li cells are assembled and charge/discharge at 1C in the voltage range of 2.8–4.3 V (Fig. 6a) and 2.8–4.5 V (Fig. 6b), respectively. With the cut-off voltage of 4.3 V, the NCA and PTNCA electrodes deliver similar initial specific capacities of 202.2 mA h g^{-1} and 205.6 mA h g^{-1} at 0.1C, respectively. However, the discharge capacity of NCA decreased to 96.5 mA h g^{-1} after 200 cycles at 1C, and the capacity retention was only 50.3%. In contrast, the discharge capacity of PTNCA was maintained at 156.4 mA h g^{-1} with a high capacity retention of 81.2% (Fig. 6a), which can be attributed to the stable surface structure of PTNCA after the plasma treatment. Similar results can be obtained with the cut-off voltage of 4.5 V (Fig. 6d). The initial specific capacity of NCA and PTNCA are increased to 239.0 mA h g^{-1} and 224.6 mA h g^{-1}, respectively, while capacity retention of PTNCA (78.0%) at 1C is much larger than that of NCA (41.7%) after 200 cycles. Moreover, rate performances of NCA and PTNCA are further studied in the voltage range of 2.8–4.3 V (Fig. 6b). The discharge

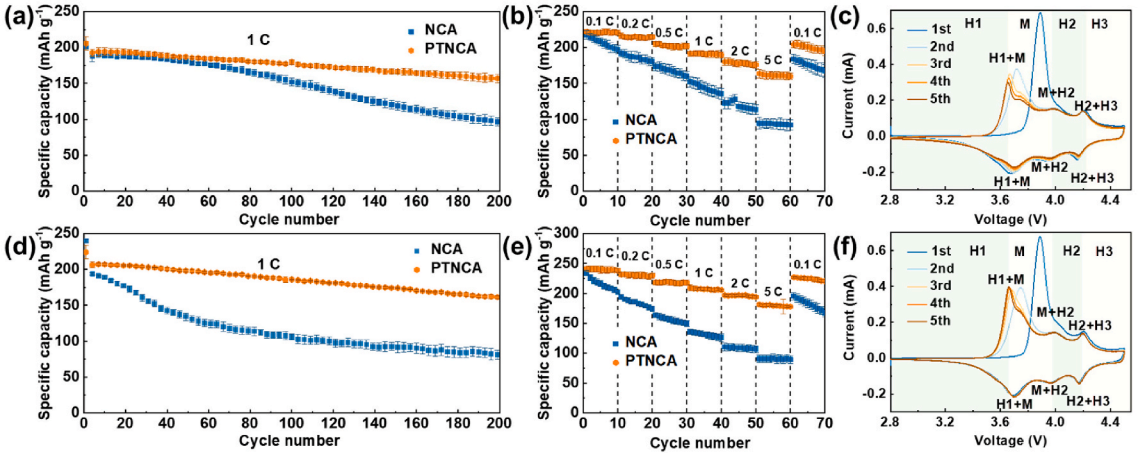

Fig. 6. a,d) Cycling performances of NCA and PTNCA at 1C with the cut-off voltage of 4.3 V and 4.5 V, respectively. b,e) Rate capacities of NCA and PTNCA with the cut-off voltage of 4.3 V and 4.5 V, respectively. c,f) Cyclic voltammetry curves of NCA and PTNCA with a scan rate of 0.1 V s^{-1}, respectively.

capacities of NCA are 205.1, 186.0, 166.6, 141.7, 117.1, and 93.3 mA h g^{-1} at current densities of 0.1, 0.2, 0.5, 1, 2, and 5C, respectively, while PTNCA exhibited the enhanced specific capacities of 221.8, 214.0, 201.2, 190.4, 178.5, and 161.1 mA h g^{-1}, respectively, which can be attributed to the improved Li^+ diffusion dynamics after plasma treatment. Similarly, in the voltage range of 2.8–4.5 V, PTNCA exhibits the improved specific capacities of 239.9, 230.7, 218.1, 207.3, 196.7, and 179.6 mA h g^{-1} than that of NCA (212.4 182.5, 154.7, 130.0, 108.5, and 90.6 mA h g^{-1}) at current densities of 0.1, 0.2, 0.5, 1, 2, and 5C, respectively. In addition, electrochemical impedance spectroscopy (EIS), to further understand the reasons for the enhanced cycle and rate performances, was performed with a frequency range of 10^{-2} Hz–10^5 Hz. As shown in Fig. S9, compared with Li/PTNCA, Li/NCA half-cell shows a greater impedance, resulting from the resistance of the rock salt on the surface to the migration of electron/charge. To insight the mechanism of electrochemical improvement of PTNCA, the structural details on the surface of NCA and PTNCA after cycling are explored by STEM-HAADF images. As shown in Fig. S8, the disordered layer can be observed on both the surface of NCA and PTNCA after 200 cycles. However, the thickness of the disordered layer on the surface of cycled PTNCA (~5 nm) is much thinner than that of cycled NCA (~13 nm), indicating a more stable layered structure formed after plasma treatment. Therefore, the adverse effects of phase transition may be limited.

To verify the effect of plasma treatment on the phase transition of Ni-rich materials during repeated charge/discharge processes, cyclic voltammetry (CV) curves of both NCA and PTNCA with a scan rate of 0.1 V s^{-1} are performed (Fig. 6c,f). Two obvious oxidation peaks, Ni^{3+} and Co^{3+}, appear at 3.88 V and 4.20 V in the first oxidation process, while these two peaks disappear in the subsequent cycles, which can be attributed to the irreversible phase transition during the first charging process, resulting in a large irreversible capacity and a low initial Coulombic efficiency. In the subsequent cycles, three pairs of redox peaks, hexagonal phase (H1)-monoclinic phase (M), M-new hexagonal phase (H2), and H2-hexagon phase (H3) appear, respectively [39]. These three pairs of redox peaks appear at ~3.65/~3.69, ~3.98/~3.96, and ~4.20/~4.16 V for NCA, as well as ~3.67/~3.7, ~3.99/~3.97, and ~4.20/~4.17 V for PTNCA, respectively. Interestingly, after the second cycle, the intensity of the oxidation peak at ~3.65 V and the reduction peak at ~4.17 V of NCA are gradually decreased, indicating that the shrinkage/expansion of the structure caused by the phase transition destroys the initial layered structure [40,41]. In contrast, the intensity of redox peaks for PTNCA are basically unchanged, indicating that the cathode material after plasma treatment possesses a more stable layered structure, which can effectively reduce the adverse effects of phase transition.

More significantly, this strategy is not only applicable to NCA, but also can be used for modification of other Ni-rich cathode materials, such as NCM. Similarly, the color of NCM precursor changed from brown to black after plasma-treated (Fig. 7a,d). In addition, the content of Ni^{3+} of NCM precursor increased from 39.1% to 55.5% after plasma treatment (Fig. 7b and c), and maintained at 61.3% after calcination, much larger than that of NCM (56.1%) (Fig. 7e and f). Furthermore, the cycle stability of NCM and PTNCM are also investigated at the current density of 1C. NCM and PTNCM exhibited similar discharge specific capacities of 187.1 mA h g^{-1} and 195.2 mA h g^{-1} at the current density of 1C under the cut-off voltage of 4.3 V, and the capacity retentions are 74.0% and 89.1% after 200 cycles, respectively. Under the cut-off voltage of 4.5 V, both NCM and PTNCM exhibited an enhanced initial discharge specific capacity of 214.5 mA h g^{-1} and 211.0 mA h g^{-1} at the current density of 1C, respectively. However, capacity retention of 88.7% can be obtained

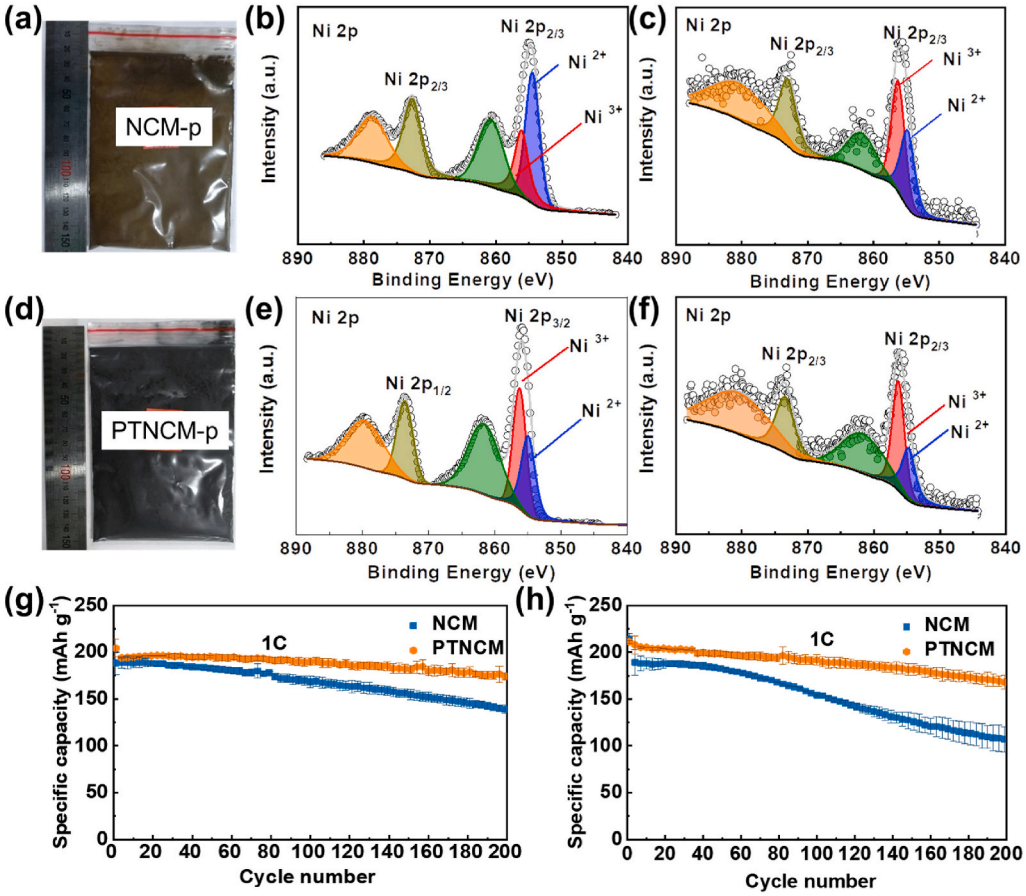

Fig. 7. a,d) Photographs of NCM-p and PTNCM-p, respectively. XPS spectra of b) NCM-p, c) NCM, e) PTNCM-p, and f) PTNCM. g,h) Cycling performances of NCM and PTNCM at 1C with the cut-off voltage of 4.3 V and 4.5 V, respectively.

in PTNCM|Li cells after 200 cycles, which is much larger than that in NCM|Li cells (56.6%), revealing the strategy of plasma treatment can be extended to other Ni-rich cathode materials.

4. Conclusion

In summary, a general and non-destructive surface reinforcement strategy has been proposed to tailor surface characteristics of precursors of Ni-rich cathode materials via plasma treatment. This surface engineering approach based on improving the surface structure and chemical properties of precursors can enhance the crystal structure of the surface of cathode and hence improve electrochemical performances. Through plasma treatment, an ideal surface with regular layered NiOOH phase can be achieved on the precursors, and the Ni-rich layered oxides without NiO-type rock-salt phase can be obtained during the following calcination process, which are proved by the spectroscopic analysis and atomic level imagings. The PTNCA cathode exhibits a high capacity retention of 81.2% after 200 cycles at 1C and enhanced rate capability (161.1 mAh g^{-1} at 5C). Furthermore, this strategy can be extend to other Ni-based cathode materials (e.g., NCM). This strategy provides guidance for the modification of layered oxide cathode materials and represent a significant progress in the development of Ni-rich cathodes for high energy density LIBs.

Declaration of competing interest

The authors declare that they have no known competing financial interests or personal relationships that could have appeared to influence the work reported in this paper.

Acknowledgements

K. Y. and N. L. contributed equally to this work.. The authors acknowledge the financial support provided by the National Natural Science Foundation of China (51974256), the Outstanding Young Scholars of Shaanxi (2019JC-12), the Natural Science Basic Research Plan in Shaanxi Province of China (2019JLZ-01 and 2019JLM-29), the Key R&D Program of Shanxi (No.2019ZDLGY04-05), the Fundamental Research Funds for the Central Universities (19GH020302 and 3102019JC005), the Innovation Foundation for Doctor Dissertation of Northwestern Polytechnical University (CX202026).The authors thank the Analytical & Testing Center of Northwestern Polytechnical University for SEM and STEM analysis.

Appendix A. Supplementary data

Supplementary data to this article can be found online at https://doi.org/10.1016/j.nanoen.2020.105239.

References

[1] F. Lin, I.M. Markus, D. Nordlund, T.C. Weng, M.D. Asta, H.L. Xin, M.M. Doeff, Nat. Commun. 5 (2014) 3529.
[2] A.T. Bell, Science 299 (2003) 1688–1691.
[3] B. Chen, L. Ben, Y. Chen, H. Yu, H. Zhang, W. Zhao, X. Huang, Chem. Mater. 30 (2018) 2174–2182.
[4] X. Xu, H. Huo, J. Jian, L. Wang, H. Zhu, S. Xu, X. He, G. Yin, C. Du, X. Sun, Adv. Energy Mater. 9 (2019), 1803963.
[5] J.B. Goodenough, Nat. Electronics 1 (2018) 204.
[6] Y. Xia, J. Zheng, C. Wang, M. Gu, Nano Energy 49 (2018) 434–452.
[7] P. Xiao, T. Shi, W. Huang, G. Ceder, ACS Energy Lett 4 (2019) 811–818.
[8] Y. Xiao, T. Liu, J. Liu, L. He, J. Chen, J. Zhang, P. Luo, H. Lu, R. Wang, W. Zhu, Z. Hu, G. Teng, C. Xin, J. Zheng, T. Liang, F. Wang, Y. Chen, Q. Huang, F. Pan, H. Chen, Nano Energy 49 (2018) 77–85.
[9] Y. Yamamoto, M. Ohtsuka, Y. Azuma, T. Takahashi, S. Muto, J. Power Sources 401 (2018) 263–270.
[10] Y. Bi, M. Liu, B. Xiao, Y. Jiang, H. Lin, Z. Zhang, G. Chen, Q. Sun, H. He, F. Huang, X. Sun, D. Wang, J.-G. Zhang, Energy Storage Materials 24 (2020) 291–296.
[11] Y. Liu, L.B. Tang, H.X. Wei, X.H. Zhang, Z.J. He, Y.J. Li, J.C. Zheng, Nano Energy 65 (2019) 104043.
[12] Y. Wei, J. Zheng, S. Cui, X. Song, Y. Su, W. Deng, Z. Wu, X. Wang, W. Wang, M. Rao, Y. Lin, C. Wang, K. Amine, F. Pan, J. Am. Chem. Soc. 137 (2015) 8364–8367.
[13] Q. Lin, W. Guan, J. Zhou, J. Meng, W. Huang, T. Chen, Q. Gao, X. Wei, Y. Zeng, J. Li, Z. Zhang, Nano Energy (2020), https://doi.org/10.1016/j.nanoen.2020.105021.
[14] Z. Tang, J. Bao, Q. Du, Y. Shao, M. Gao, B. Zou, C. Chen, ACS Appl. Mater. Interfaces 8 (2016) 34879–34887.
[15] M.J. Zhang, G. Teng, Y.K. Chen-Wiegart, Y. Duan, J.Y.P. Ko, J. Zheng, J. Thieme, E. Dooryhee, Z. Chen, J. Bai, K. Amine, F. Pan, F. Wang, J. Am. Chem. Soc. 140 (2018) 12484–12492.
[16] C.K. Yang, L.Y. Qi, Z. Zuo, R.N. Wang, M. Ye, J. Lu, H.H. Zhou, J. Power Sources 331 (2016) 487–494.
[17] H.H. Li, N. Yabuuchi, Y.S. Meng, S. Kumar, J. Brege, C.P. Grey, Y.S. Hong, Chem. Mater. 19 (2007) 2551–2565.
[18] S. Hwang, W. Chang, S. Kim, D. Su, D. Kim, J. Lee, K. Chung, E. Stach, Chem. Mater. 26 (2014) 1084–1092.
[19] C.C. Zhang, M.M. Liu, G.J. Pan, S.Y. Liu, D. Liu, C.G. Chen, J.M. Su, T. Huang, A. S. Yu, ACS Appl. Energy Mater. 1 (2018) 4374–4384.
[20] B. Huang, X.H. Li, Z.X. Wang, H.J. Guo, L. Shen, J.X. Wang, J. Power Sources 252 (2014) 200–207.
[21] Q. Zhang, Y. Su, L. Chen, Y. Lu, L. Bao, T. He, J. Wang, R. Chen, J. Tan, F. Wu, J. Power Sources 396 (2018) 734–741.
[22] B. Huang, M. Wang, X. Yang, G. Xu, Y. Gu, J. Alloys Compd. 808 (2019), 151683.
[23] B. Huang, M. Wang, Z. Zhao, L. Chen, Y. Gu, J. Alloys Compd. 810 (2019), 151800.
[24] S. Ahmed, A. Pokle, S. Schweidler, A. Beyer, M. Bianchini, F. Walther, A. Mazilkin, P. Hartmann, T. Brezesinski, J. Janek, K. Volz, ACS Nano 13 (2019) 10694–10704.
[25] J.F. Zhu, J. Chen, Y. Luo, S.Q. Sun, L.G. Qin, H. Xu, P.G. Zhang, W. Zhang, W. B. Tian, Z.M. Sun, Energy Storage Mater 23 (2019) 539–546.
[26] S.M. Kang, J.J. Koo, H.M. Seo, Q.T. Truong, J.B. Park, S.C. Park, Y. Jung, S.P. Cho, K.T. Nam, Z.H. Kim, B.H. Hong, J. Mater. Chem. C 7 (2019) 10173–10178.
[27] K.M. Price, S. Najmaei, C.E. Ekuma, R.A. Burke, M. Dubey, A.D. Franklin, ACS Appl. Nano Mater. 2 (2019) 4085–4094.
[28] Y. Mo, L. Guo, B. Cao, Y. Wang, L. Zhang, X. Jia, Y. Chen, Energy Storage Mater 18 (2019) 260–268.
[29] J. Maruta, H. Yasuda, M. Yamachi, J. Power Sources 90 (2000) 89–94.
[30] J. Li, A.R. Cameron, H.Y. Li, S. Glazier, D.J. Xiong, M. Chatzidakis, J. Allen, G. A. Botton, J.R. Dahn, J. Electrochem. Soc. 164 (2017) A1534–A1544.
[31] H.Y. Li, J. Li, X.W. Ma, J.R. Dahn, J. Electrochem. Soc. 165 (2018) A1038.
[32] S.K. Jung, H. Gwon, J. Hong, K.Y. Park, D.H. Seo, H. Kim, J. Hyun, W. Yang, K. Kang, Adv. Energy Mater. 4 (2014), 1300787.
[33] G.R. Hu, W.M. Liu, Z.D. Peng, K. Du, Y.B. Cao, J. Power Sources 198 (2012) 258–263.
[34] T.P. Gao, K.W. Wong, K.Y. Fung, W. Zhang, K.M. Ng, Electrochim. Acta 288 (2018) 153–164.
[35] W. Liu, P. Oh, X. Liu, M.J. Lee, W. Cho, S. Chae, Y. Kim, J. Cho, Angew Chem. Int. Ed. Engl. 54 (2015) 4440–4457.
[36] Y. Cho, S. Lee, Y. Lee, T. Hong, J. Cho, Adv. Energy Mater. 1 (2011) 821–828.
[37] A.N. Mansour, C.A. Melendres, Surf. Sci. Spectra 3 (1994) 271–278.
[38] A.N. Mansour, Surf. Sci. Spectra 3 (1994) 239–246.
[39] P.F. Zhou, H.J. Meng, Z. Zhang, C.C. Chen, Y.Y. Lu, J. Cao, F.Y. Cheng, J. Chen, J. Mater. Chem. A 5 (2017) 2724–2731.
[40] U.H. Kim, H.H. Ryu, J.H. Kim, R. Mücke, P. Kaghazchi, C.S. Yoon, Y.K. Sun, Adv. Energy Mater. 9 (2019), 1803902.
[41] K.J. Park, M.J. Choi, F. Maglia, S.J. Kim, K.H. Kim, C.S. Yoon, Y.K. Sun, Adv. Energy Mater. 8 (2018), 1703612.

Kai Yuan: is currently a Ph.D. candidate in School of Materials Science and Engineering, Northwestern Polytechnical University under the supervision of Prof. Keyu Xie. His current research focuses on the design, synthesis as well as performance improvement and structural characterization of Ni-rich cathode materials for high performance lithium ion batteries.

Nan Li: is currently a Ph.D. student in School of Materials Science and Engineering, Northwestern Polytechnical University. Her research focuses on design and synthesis of electrode materials for rechargeable batteries (e.g. Li-ion batteries, Li metal batteries, Na-ion batteries).

Ruiqi Ning: is currently a M. S. candidate in materials science under the supervision of Prof. Keyu Xie in School of Materials Science and Engineering, Northwestern Polytechnical University. Her research focuses on the design, synthesis as well as performance improvement of Ni-based layered cathode materials of lithium-ion batteries.

Chao Shen: received his Ph.D. degree from Central South University in 2015. Currently, he is working at Northwestern Polytechnical University as an associate researcher. His research interests focus on electrode materials and devices for advanced batteries.

Nan Hu: received his M. S. degree in 2020 from Northwestern Polytechnical University. His research interests focus on the design, synthesis as well as performance improvement of Ni-based cathode materials for high performance lithium ion batteries.

Maohui Bai: received his Ph.D. degree in 2019 from Central South University. His research interests focus on the design as well as performance improvement of electrode materials for rechargeable batteries, especially for Li metal batteries.

Kun Zhang received his B.E. (2015) and M.S. (2018) degrees in Material Science from Northwestern Polytechnical University. Now he is a PhD candidate under the supervision of Prof. Keyu Xie in the Center for nano energy materials at Northwestern Polytechnical University. His research interests mainly focus on lithium metal and lithium sulfur batteries.

Zhanyuan Tian: received his M. S. degree from Zhejiang University in 2010. And he is currently a Ph.D. candidate for a PhD degree in Xi'an Jiaotong University. He is a researcher of New Energy Technology Department, Shaanxi Coal and Chemical Technology Institute Co., Ltd. His research interests focus on the negative and positive materials and the rational design for lithium ion batteries.

Le Shao: received his Ph.D. degree from Shanghai Institute of Ceramics, Chinese Academy of Sciences in 2013. Currently, he is a researcher of New Energy Technology Department, Shaanxi Coal and Chemical Technology Institute Co., Ltd. He works on the design and manufacturing for lithium ion batteries.

Zhaowen Hu: is a Ph.D. student in School of Materials Science and Engineering, Northwestern Polytechnical University. Currently, he is a researcher of New Energy Technology Department, Shaanxi Coal and Chemical Technology Institute Co., Ltd. His research interests focus on the design, synthesis, as well as characterization of cathode materials for lithium ion batteries.

Xin Xu: received his Ph.D. from Xi'an Jiaotong University in 2016, and worked as a postdoctoral fellow at Nanyang Technological University in Singapore from 2016 to 2020. Dr. Xu currently works at school of electrical engineering, Xi'an Jiaotong University as a faculty member. His research focuses on the electrode materials for lithium ion, sodium ion, and potassium ion batteries, supercapacitor, as well as photocatalysis.

Ting Yu: received his Ph.D. from Department of Physics, National University of Singapore in 2003. Dr. Yu is currently a professor in the school of physical and mathematical sciences, Nanyang Technological University in Singapore. His research interests cover fabrication of low dimensional, especially 2D materials and investigation of their optical, optoelectrical and electrochemical properties for developing novel electronics, optoelectronics and energy conversion/storage. Dr Yu has published more than 280 SCI papers and received over 23,000 nonself-citations. His H-index is 82. Dr Yu has been selected as Highly Cited Researcher 2017–2019.

Keyu Xie: received his Ph.D. degrees from Central South University in 2012. Dr. Xie is currently a full professor at Center for Nano Energy Materials, School of Materials Science and Engineering, Northwestern Polytechnical University. His research focuses on energy materials and battery electrochemistry (advanced secondary batteries such as lithium ion batteries, lithium sulfur batteries, sodium ion batteries, etc.)